

Epitaxial TiO2 Shell Grown by Atomic Layer Deposition on ZnO Nanowires Using a Double-Step Process and Its Beneficial Passivation Effect

Thomas Cossuet, Estelle Appert, Odette Chaix-Pluchery, Herve Roussel, Laetitia Rapenne, Gilles Renou, Frédéric Sauvage, Vincent Consonni

▶ **To cite this version:**

Thomas Cossuet, Estelle Appert, Odette Chaix-Pluchery, Herve Roussel, Laetitia Rapenne, et al.. Epitaxial TiO2 Shell Grown by Atomic Layer Deposition on ZnO Nanowires Using a Double-Step Process and Its Beneficial Passivation Effect. Journal of Physical Chemistry C, 2020, 124 (24), pp.13447-13455. 10.1021/acs.jpcc.0c02605 . hal-02994844

HAL Id: hal-02994844
https://hal.science/hal-02994844

Submitted on 26 Nov 2020

HAL is a multi-disciplinary open access archive for the deposit and dissemination of scientific research documents, whether they are published or not. The documents may come from teaching and research institutions in France or abroad, or from public or private research centers.

L'archive ouverte pluridisciplinaire **HAL**, est destinée au dépôt et à la diffusion de documents scientifiques de niveau recherche, publiés ou non, émanant des établissements d'enseignement et de recherche français ou étrangers, des laboratoires publics ou privés.

Epitaxial TiO_2 Shell Grown by Atomic Layer Deposition on ZnO Nanowires Using a Double-Step Process and Its Beneficial Passivation Effect

Thomas Cossuet,[1] Estelle Appert,[1] Odette Chaix-Pluchery,[1] Hervé Roussel,[1] Laetitia Rapenne,[1] Gilles Renou,[2] Frédéric Sauvage,[3] and Vincent Consonni.[1*]

[1] *Univ. Grenoble Alpes, CNRS, Grenoble INP, LMGP, F-38000 Grenoble, France*

[2] *Univ. Grenoble Alpes, CNRS, Grenoble INP, SIMaP, F-38042 Saint-Martin d'Hères, France*

[3] *Laboratoire de Réactivité et Chimie des Solides, Université de Picardie Jules Verne, CNRS UMR7314, 33 Rue St-Leu, 80039 Amiens cedex, France*

*Corresponding Author:

Vincent Consonni

LMGP, Grenoble INP – Minatec, 3 parvis Louis Néel – CS 50257 – 38016 Grenoble cedex 1

Tel : (+33) 456529358

vincent.consonni@grenoble-inp.fr

ABSTRACT

Owing to the chemical instability of ZnO nanowires and to its large surface area exhibiting a high density of traps, the use of a protective, passivating shell plays a major role on the performances of the related devices. We show that a conformal TiO_2 shell can be grown on the ZnO nanowires by a double-step process using atomic layer deposition and post-deposition thermal treatment in air. An *in situ* analysis of the crystallisation process of the amorphous TiO_x shell grown by atomic layer deposition is achieved in details by temperature-dependent Raman scattering and x-ray diffraction measurements, indicating that the crystallization starts around 280 °C in air and that only the anatase phase is formed. It is further revealed from transmission electron microscopy-based experiments that the TiO_2 shell with the anatase phase is epitaxially grown on the ZnO nanowires with a range of orientation relationships. Interestingly, the epitaxial TiO_2 shell has a beneficial passivating effect and results in the redistribution of the hydrogen-related defects in the center of ZnO nanowires following the post-deposition thermal treatment at 350 °C, as shown by steady-state and time-resolved photoluminescence measurements. These findings demonstrate that the atomic layer deposition technique coupled with a post-deposition thermal treatment is a powerful tool to form ZnO / TiO_2 core-shell nanowire heterostructures with high structural and optical quality. They open the way for developing the present double-step process in other nanostructured material systems to master their related surface and interface properties.

1. INTRODUCTION

ZnO nanowires (NWs) have received an overwhelming interest in the last decade for their integration into a large variety of nanoscale devices in the fields of piezoelectricity,[1] optoelectronics,[2-3] photovoltaics,[4] detection, and sensing.[5] In most of these devices, the control of the surface properties of ZnO NWs exhibiting a high aspect ratio at nanoscale dimensions is a critical issue, because their performances are largely governed by the different interfaces in the system. Owing to the high density of surface traps lying in the range of 10^{12} - $5x10^{13}$ cm^{-2} [6-7] as well as to its chemical instability over a broad range of conditions in solution and gas phases, the covering of ZnO NWs by a TiO_2 shell using atomic layer deposition (ALD) has been considered for many devices, specifically in the fields of photovoltaics and photo-catalysis. The present combination is also favorable in these devices thanks to the type II band alignment between ZnO and TiO_2.[8] The insertion of a TiO_2 shell by ALD in dye-sensitized solar cells made of ZnO NWs has been reported to drastically increase the open-circuit voltage and fill factor, enhancing the photo-conversion efficiency up to 7.0 % by improving the interface with the dye.[9-16] Similarly, Parize *et al.* showed that the extremely thin absorber solar cells made of ZnO / Sb_2S_3 core-shell NW heterostructures have an enhanced performance when a TiO_2 shell deposited by ALD is inserted, leading to a photo-conversion efficiency of up to 2.3 %.[17] Cheng *et al.* showed that the insertion of a TiO_2 shell deposited by ALD on ZnO NWs resulted in the increase in the short-circuit current density and photo-conversion efficiency in bulk heterojunction quantum dot solar cells incorporating PbS quantum dots, indicating the improvement of the charge carrier collection.[18] The same enhancement has been reported in ZnO NW-based hybrid solar cells with P3HT[19-21] and in ZnO NW-based halide perovskite solar cells to reach a photo-conversion efficiency of 14.35 % [22-23] by using a TiO_2 shell. Additionally, the photocatalytic activity of ZnO / TiO_2 core-shell NW heterostructures has been shown to outperform the one of bare ZnO NW arrays.[24-25] Eventually, the much higher chemical stability

of TiO_2 has been used to combine ZnO NWs with a large number of materials grown in acidic, corrosive conditions in order to benefit from their high aspect ratio.[26] Overall, the TiO_2 shell grown by ALD on ZnO NWs has been found to be polycrystalline with a varying degree of crystallinity with the purposes of passivating the surface traps together with improving their chemical stability. However, the comprehensive role of the TiO_2 shell including the effects of its crystalline phase, its crystallization process, and the related interface properties with ZnO NWs is still under debate despite its primary importance in the performances of the devices.

In order to address that issue, an *in situ* analysis of the crystallization process of the TiO_2 shell grown by ALD on ZnO NWs is achieved by temperature-dependent Raman scattering and x-ray diffraction (XRD) measurements. The interface properties of the resulting ZnO / TiO_2 core-shell NW heterostructures are investigated in details by transmission electron microscopy (TEM)-based experiments as well as steady-state and time-resolved photoluminescence (PL) measurements. It is shown that the TiO_2 shell with the anatase phase can epitaxially be formed on ZnO NWs by combining ALD with post-deposition thermal treatment in air, resulting in the fabrication of high quality ZnO / TiO_2 core-shell NW heterostructures with improved interface properties.

2. EXPERIMENTAL SECTION

ZnO NW arrays were grown on *c*-axis oriented polycrystalline ZnO seed layers deposited on (001) silicon wafers, using a two-step chemical synthesis process. First, the polycrystalline ZnO seed layers were deposited by the sol-gel process using dip coating. To form the sol, 375 mM of zinc acetate dihydrate ($Zn(CH_3COO)_2.2H_2O$, Sigma-Aldrich) and 375 mM of monoethanolamine (MEA, Sigma-Aldrich) were mixed in pure ethanol. The solution was heated and stirred at 60 °C for 12 hours, and then at room temperature for 12 more hours. To form the xerogel film, silicon wafers were dipped in the solution and withdrew at the speed of 3.3 mm/s in ambient atmosphere with a hygrometry smaller than 15 %. The xerogel film was

annealed in air on a hot plate kept at 300 °C for 1 hour, and on another hot plate kept at 500 °C for 3 hours. Second, the ZnO seed layer-coated silicon wafers were immersed face down in a sealed beaker containing an equimolar mix of 30 mM of zinc nitrate hexahydrate ($Zn(NO_3)_2.6H_2O$, Sigma-Aldrich) and HMTA ($C_6H_{12}N_4$, Sigma-Aldrich) in deionized water. The sealed beaker containing the solution was placed in a regular oven heated at 90 °C for 3 hours.

The TiO_2 shell was subsequently grown on ZnO NW arrays at 200 °C by atomic layer deposition (ALD) using a F200 Fiji reactor from Cambridge Nanotech. Tetrakis dimethylamino titanium (TDMAT) heated at 75°C as titanium precursor and H_2O as oxygen precursor were carried in the chamber by argon gas. Sequential pulses of TDMAT and H_2O of 0.1 second followed by a purge of 10 seconds after each pulse were achieved to alternately inject titanium and oxygen precursors, respectively. The chamber pressure was set to 110 mTorr and increased up to 210 mTorr as the pulse proceeded. A complete sequence of 150 cycles was carried out to form an amorphous TiO_x shell on ZnO NW arrays. Post-deposition thermal treatment in air was performed using an annealing temperature of 250, 350, and 500 °C for 3 hours.

The morphology of ZnO / TiO_2 core-shell NW heterostructures was studied by top-view and cross-sectional view field-emission scanning electron microscopy (FESEM) imaging using a ZEISS Ultra FEG-SEM. TEM specimens were prepared by scratching the ZnO / TiO_2 core-shell NW heterostructures using a diamond tip and put on Holey Carbon copper grid. TEM and HRTEM images were recorded with a JEOL JEM 2010 LaB_6 microscope operating at 200 kV with a 0.19 nm point-to-point resolution. EDS mapping was collected by STEM with a JEOL 2100F FEG microscope operating at 200 kV with a 0.2 nm resolution in the scanning mode and equipped with a JEOL SDD Centurio detector with a large solid angle of up to 0.98 steradians. The local structural properties of the ZnO / TiO_2 core-shell NW heterostructures were further investigated by using an automated crystal phase and orientation mapping (ACOM) with

precession (ASTAR) system implemented in the JEOL 2100F FEG microscope. The crystal phase and orientation maps were obtained by precession of the primary electron beam around the microscope's optical axis at an angle of 1.16° while collecting the electron diffraction patterns at a rate of 100 frames per second with a step size of 1 nm.

In situ and *ex situ* Raman scattering measurements were performed using a Jobin Yvon/Horiba Labram spectrometer equipped with a liquid nitrogen cooled charge-coupled device detector. The 488 nm excitation line of an Ar^+ laser with a power around 2 mW at the sample surface was used. The light was focused to a spot size close to 1 μm^2 using a 50x long working distance objective. Raman spectra were calibrated at room temperature using a silicon reference sample with a theoretical position of 520.7 cm^{-1}. The annealing temperature was controlled using a commercial Linkam heating stage (THMS600) placed under the Raman microscope, and varied in the range of 20 – 600 °C. *In situ* and *ex situ* XRD measurements were performed with a Rigaku SmartLab diffractometer and a Bruker D8 Advance diffractometer, respectively, using the $CuK\alpha_1$ radiation according to the Bragg-Brentano configuration. The annealing temperature was controlled using an Anton Paar DHS 1100 chamber, and varied in the range of 20 – 600 °C. *In situ* Raman spectra and XRD patterns were recorded with an acquisition time varying from 5 to 10 min depending on the annealing temperature.

Steady-state and time-resolved photoluminescence (PL) studies were carried out using an Edinburgh Instrument FLS980 spectrometer in front-face configuration. The steady-state PL spectra were measured with a continuous ozone-free xenon arc lamp (450 W) for excitation in a double grating Czerny-Turner monochromator for both excitation part and emission part to reach a total stray light rejection to less than $1:10^{-10}$. Both excitation / emission slits were opened to a bandwidth of 3 nm for steady state. The emission was detected at 90° from excitation by means of a high-gain Hamamatsu photomultiplier tube (PMT) detector mounted after the second emission monochromator. The time-resolved PL experiments were performed in single

photon counting mode using a picosecond 375 nm laser diode as an excitation source (2 MHz) and a microchannel plate PMT (MCP-PMT) Hamamatsu detector cooled at -20°C. This latter was settled after the first emission monochromator to minimize instrumental time resolution down to ca. 80 ps time scale. The slit opening of the excitation monochromator was 10 nm wide to maximize the photon counting. A long pass filter of 410 nm was used to avoid the counting of incident photons directly reflected by the samples without being rejected by the monochromator. The laser energy was ca. 100 nJ/cm^2.

3. RESULTS AND DISCUSSION

3.1. Morphology and structural properties of ZnO / TiO_2 core-shell nanowire heterostructures.

The structural morphology of ZnO / TiO_2 core-shell NW heterostructures annealed at 350 °C for 3 hours in air is presented in **Figure 1**. ZnO NWs grown by CBD on a *c*-axis oriented polycrystalline ZnO seed layer by sol-gel process[27] exhibit a mean diameter and length of 81 ± 22 nm and 892 ± 102 nm, respectively, using an equimolar mix of zinc nitrate and HMTA.[28] They retain the typical hexagonal facet on their top face following the ALD of the TiO_2 shell. However, the surfaces on their *c*-plane top face and *m*-plane sidewalls have a granular morphology indicating the formation of the TiO_2 shell. No change in the structural morphology of ZnO / TiO_2 core-shell NW heterostructures before and after annealing has been revealed by FESEM imaging.

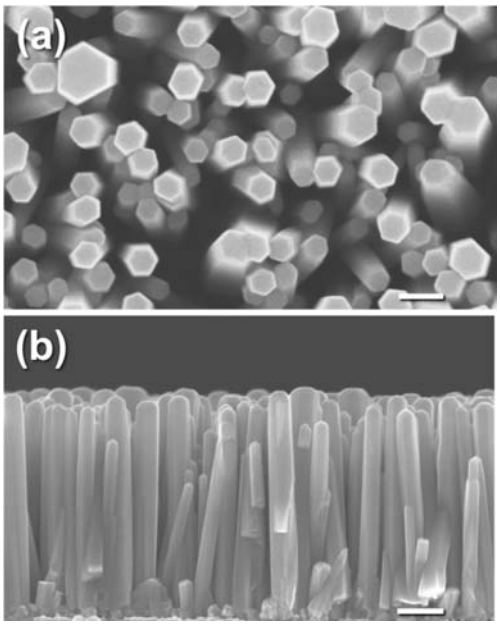


Figure 1. (a) Top-view and (b) cross-sectional view FESEM images of ZnO / TiO_2 core-shell NW heterostructures annealed at 350 °C for 3 hours in air. The scale bars denote 100 and 200 nm, respectively.

3.2. In situ analysis of the crystallization process of TiO_2 shell. *In situ* Raman scattering and XRD measurements were performed from room temperature (RT) to 600 °C to thoroughly investigate the transformation of the amorphous TiO_x shell into the crystallized TiO_2 shell during the crystallization process. The corresponding *in situ* Raman spectra and XRD patterns recorded in air from RT to 600 °C, and after cooling down, are presented in **Figures 2** and **3**, respectively.

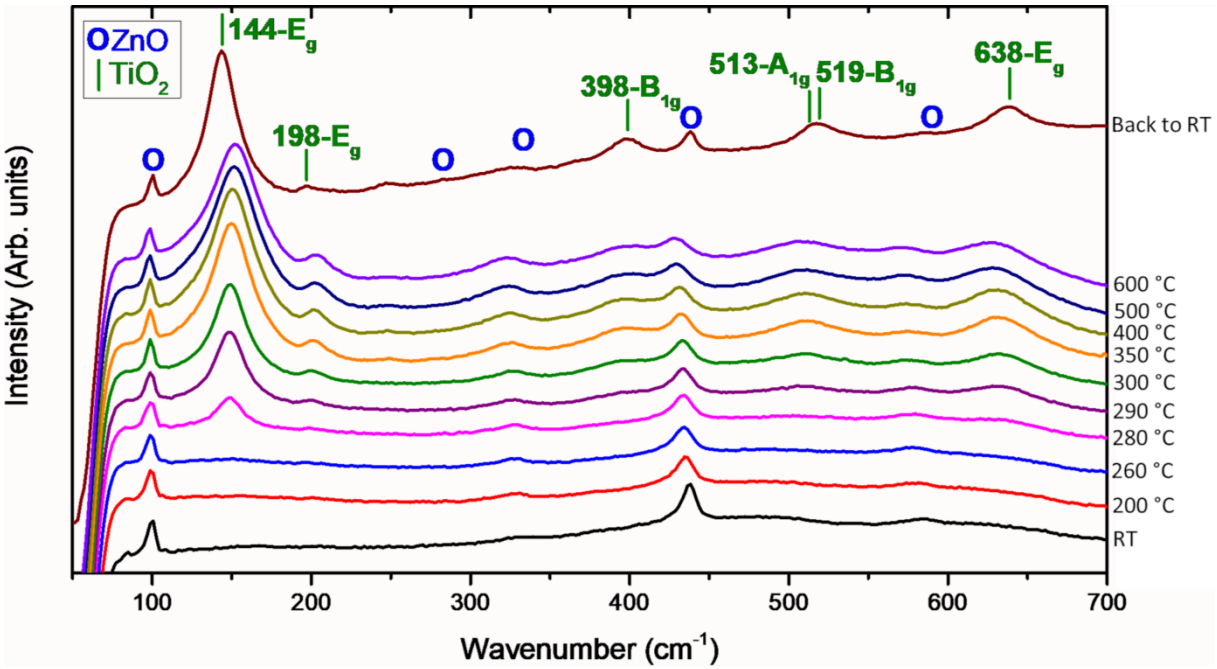


Figure 2. *In situ* Raman spectra of ZnO / TiO_2 core-shell NW heterostructures annealed from RT to 600 °C in air.

Prior to post-deposition thermal treatment, several well-defined lines occur in the Raman spectrum and are typically attributed to the wurtzite phase of ZnO NWs. Two intense lines at 100 and 438 cm^{-1} are assigned to the E_2^{low} and E_2^{high} modes, respectively, while the much weaker lines at 333 and 590 cm^{-1} are due to the E_2^{high}-E_2^{low} and E_1(LO) modes, respectively.[29] Correlatively, the diffraction peak at 34.4° is mostly ascribed to the (002) plane of the wurtzite phase of ZnO NWs. The diffraction peaks at 31.8, 36.3, 56.8, and 62.9° entirely correspond to the (100), (101), (110), and (103) planes of the wurtzite phase of polycrystalline ZnO seed layer.[27] The Raman spectra and XRD patterns recorded from RT to 260°C are very similar to each other, showing that no drastic change occurs in the amorphous TiO_x shell and thus that the crystallization process has not started in that annealing temperature range.

At the annealing temperature of 280 °C, an additional line at 149 cm^{-1} occurs in the Raman spectrum. It is assigned to the low-frequency E_g mode of the anatase phase of the TiO_2 shell.[30] Correlatively, a small shoulder occurs in the XRD pattern with a diffraction peak around 37.9° corresponding to the (004) plane of the anatase phase of the TiO_2 shell. The start of the

crystallization process of the TiO_x shell thus proceeds at 280 °C through the formation of the anatase phase. In the range of 280 to 600 °C, the intensity of the Raman line at 149 cm^{-1} is much more pronounced and typically shifts towards higher wavenumbers while broadening, as expected from its temperature dependence.[31] Also, the additional lines at 198, 398, 513, 519, and 638 cm^{-1} progressively occur in the Raman spectrum and are assigned to the E_g, B_{1g}, A_{1g}, B_{1g}, and E_g modes, respectively, corresponding to the anatase phase of the TiO_2 shell.[30] Correlatively, the intensity of the diffraction peak around 37.9° slightly increases in the range of 280 to 600 °C. This indicates that the crystallization process of the TiO_2 shell is more active and that its crystallinity is improved in that annealing temperature range. After cooling down, all the phonon modes corresponding to the anatase phase of the TiO_2 shell are clearly shown in the wavenumber range of 100 – 700 cm^{-1} while the diffraction peak around 37.9° occurs, revealing that the crystallization process has efficiently been proceeded. No sign for the presence of the rutile/rocksalt phases of TiO_2 is indicated, showing that the shell has crystallized into the pure anatase phase.

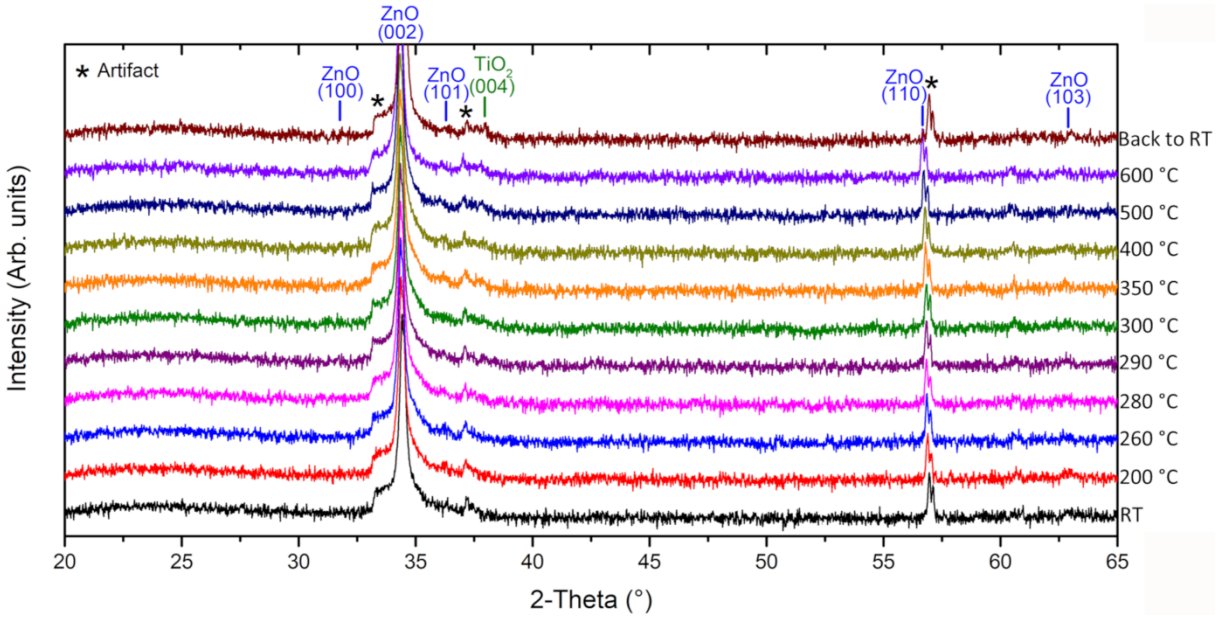


Figure 3. *In situ* XRD patterns of ZnO / TiO_2 core-shell NW heterostructures annealed from RT to 600 °C in air.

An *ex situ* post-deposition thermal treatment of the amorphous TiO_x shell on ZnO NWs was achieved at 250, 350, and 500 °C for 3 hours in air to corroborate the *in situ* analysis. The corresponding XRD patterns and Raman spectra are presented in **Figure S1** and **S2**. The XRD pattern reveals that the TiO_x shell is still amorphous following the post-deposition thermal treatment at 250 °C with no sign for the presence of diffraction peaks. In contrast, the E_g line at 144 cm^{-1} of the anatase phase already occurs in the Raman spectrum, giving direct evidence of the crystallization onset that is likely localized highly. The longer annealing time as compared to the *in situ* analysis is thus sufficient to very locally activate the crystallization, showing the importance of kinetic phenomena in that process. After thermal treatments at 350 and 500 °C, both techniques show that the TiO_2 shell is well crystallized into the anatase phase, as shown by the occurrence of the diffraction peaks at 25.3, 37.9, 38.6, and 48.1° that are assigned to the (101), (004), (112) and (200) planes, as well as of the Raman lines at 144, 198, 398, 513, 519, 638 cm^{-1} that correspond to the E_g, E_g, B_{1g}, A_{1g}, B_{1g}, E_g modes, respectively.[30] It should be noted here that the post-deposition thermal treatment in the range of 280 – 350 °C is compatible with the use of glass covered with a transparent conductive oxide layer as a typical substrate in the field of photovoltaics. It is not the case for the post-deposition thermal heat treatment above 500 °C. Also, the integration of an amorphous TiO_2 shell is not favorable for the charge carrier separation in such nanostructured solar cells.[4] In the following, the interface properties between the ZnO NWs and TiO_2 shell are thus investigated in details for the most appropriate condition using the post-deposition thermal treatment at 350 °C.

3.3. Interface properties between the ZnO nanowires and TiO_2 shell. TEM and HRTEM images of a ZnO / TiO_2 core-shell NW heterostructure annealed at 350 °C for 3 hours in air are presented in **Figure 4**. The deposition of the TiO_2 shell on the *m*-plane sidewalls of ZnO NW is highly conformal with a constant thickness of 8.5 nm from its top to its bottom, as revealed in the TEM image of **Figure 4a**. The thickness of the TiO_2 shell on the *c*-plane face

of ZnO NW is however slightly larger. The HRTEM image in **Figure 4b** collected close to the ZnO / TiO_2 interface reveals the alignment of the (0002) plane of the ZnO NW with the (004) plane of the TiO_2 shell. The related SAED pattern in **Figure 4c** confirms that the ZnO NW and TiO_2 shell crystallize into the wurtzite and anatase phases, respectively. It further shows that the TiO_2 shell has an orientation relationship with the ZnO NW, following the post-deposition thermal treatment at 350 °C in air.

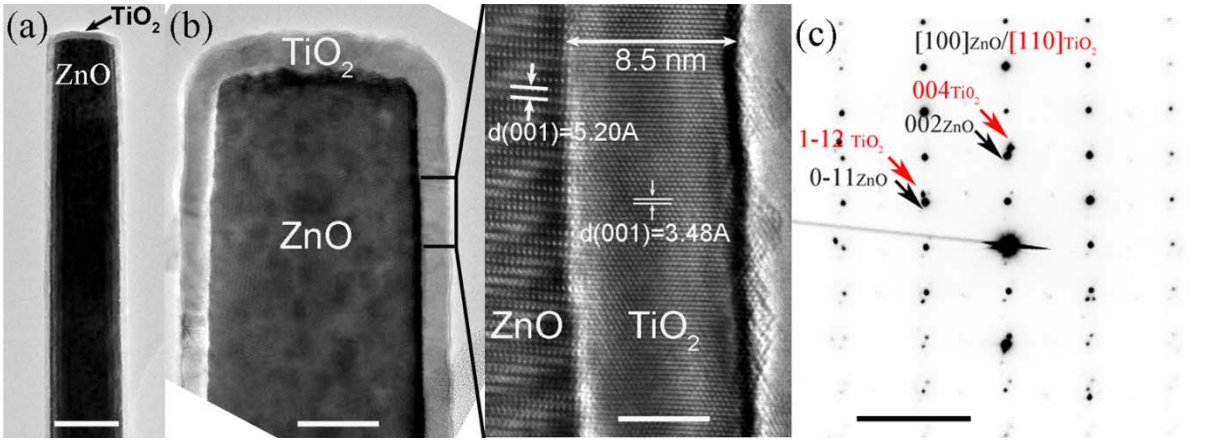


Figure 4. (a) TEM image of a ZnO / TiO_2 core-shell NW heterostructure after annealing at 350 °C for 3 hours in air (i.e., scale bar = 100 nm). (b) Corresponding TEM image of ZnO / TiO_2 core-shell NW heterostructure at higher magnification (i.e., scale bar = 25 nm). The inset on the right hand side shows a HRTEM image of the ZnO / TiO_2 interface (i.e., scale bar = 5 nm). (c) Corresponding SAED pattern revealing the ZnO wurtzite and TiO_2 anatase structures of both phases (i.e., scale bar = 5 nm^{-1}).

Owing to the inherent spatial localization of the HRTEM imaging on the nanometer scale, the structural properties of the TiO_2 shell and the related ZnO / TiO_2 interface properties were investigated on a larger scale by ASTAR measurements.[32-33] In this technique, the incident electron beam had a few nanometers in size and was precessed to reduce dynamical effects and to enhance the indexing quality. The electron beam was simultaneously scanned over the area of interest to record an electron diffraction pattern at each location. The experimental electron

diffraction patterns were basically compared with the complete set of theoretical diffraction patterns, which were computed for every expected crystalline phases and for a large number of orientations. The best match between the experimental and theoretical electron diffraction patterns permitted to identify both crystalline phase and orientation with a high precision.[34] The maps of the crystalline phases and orientations of ZnO / TiO_2 core-shell NW heterostructures are presented in **Figures 5** and **6**, respectively.

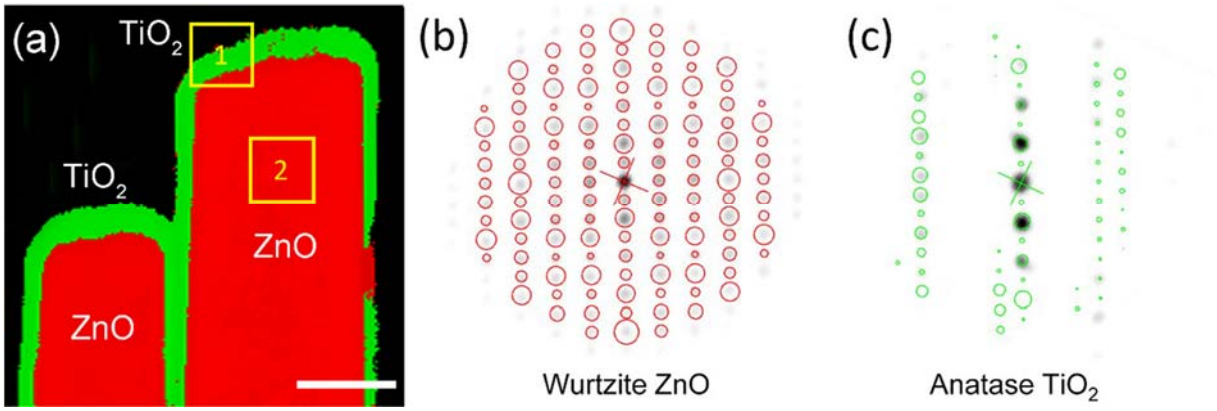


Figure 5. (a) ASTAR map representing the crystalline phases of ZnO / TiO_2 core-shell NW heterostructures annealed at 350 °C for 3 hours in air (i.e., scale bar = 50 nm). The ZnO wurtzite and TiO_2 anatase phases are shown in red and green, respectively. (b, c) Corresponding electron diffraction patterns collected at points (1) and (2), respectively. The red and green open circles represent the theoretical electron diffraction patterns of wurtzite ZnO and anatase TiO_2, respectively.

It is clearly shown in **Figure 5** that the TiO_2 shell on the *m*-plane sidewalls and *c*-plane face of ZnO NW exclusively crystallizes into the anatase phase, which is in agreement with the previous Raman scattering and XRD measurements. No sign for the presence of a residual amorphous phase or of rutile/rocksalt phases or of Zn_2TiO_4 spinel phase is indicated.[35] Also, the orientation map in **Figure 6** reveals that the TiO_2 shell is epitaxially formed on the *m*-plane sidewalls and *c*-plane face of the ZnO NW located on the left. The orientation relationship between the TiO_2 shell and *c*-plane face of ZnO NW is the following: the (001) and (0001)

planes as well as the (120) and $(10\bar{1}0)$ planes are parallel to each other with only a very small misorientation. The orientation relationship between the TiO_2 shell and *m*-plane sidewalls of the ZnO NW is identical and as follows: the (120) and $(10\bar{1}0)$ planes as well as the (001) and (0001) planes are parallel to each other with only a very small misorientation also. It is worth noticing that the lattice mismatch between the TiO_2 and ZnO materials lies in the range of 10 % in both orientation configurations, indicating that the epitaxial strain has completely been relieved plastically during the post-deposition thermal treatment. In contrast, the TiO_2 shell formed on the *m*-plane sidewalls and *c*-plane face of nearby ZnO NW located on the right is slightly more inhomogeneous and typically exhibits a local epitaxy with a large number of orientation relationships. Overall, the present finding shows that the epitaxial deposition of the TiO_2 shell can be achieved by ALD followed by a post-deposition thermal treatment according to a double-step process, which is remarkable to get high quality ZnO / TiO_2 core-shell NW heterostructures. The orientation relationships are however multiple and the local epitaxy is inevitably relieved totally. It should be noted here that the epitaxial deposition by ALD has only been reported a few times in the literature regarding a couple of dedicated materials systems in a thin film configuration including TiO_2 / Al_2O_3.[36] The structural quality of epitaxial TiO_2 shell is nevertheless dependent to a small extent upon the considered ZnO NW because the deposit of the TiO_x shell by ALD is likely affected by the varying free space between the nearby ZnO NWs.

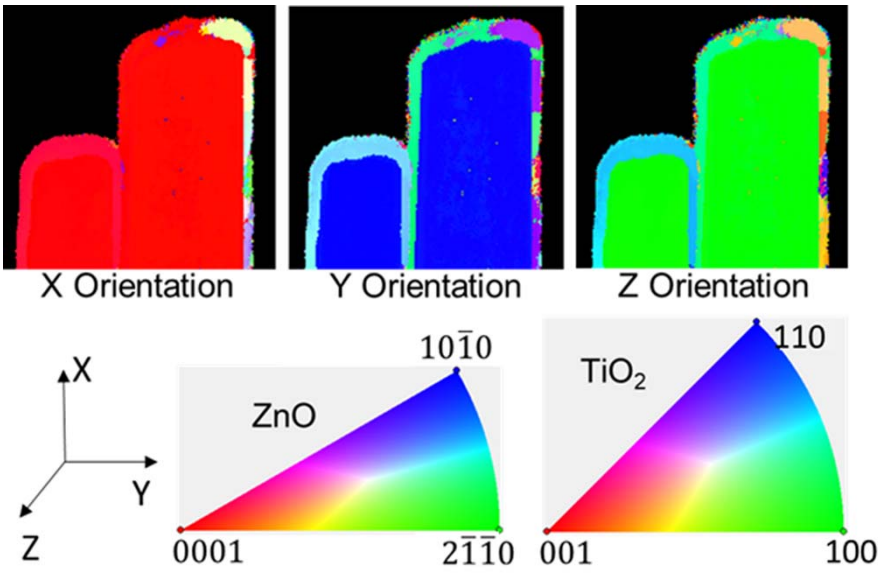


Figure 6. ASTAR maps representing the crystalline orientations of the wurtzite ZnO and anatase TiO_2 phases within the ZnO / TiO_2 core-shell NW heterostructure annealed at 350 °C for 3 hours in air, plotted along the X, Y and Z axes. The color scales for the wurtzite ZnO and anatase TiO_2 phases are given in the insets.

Steady-state and time-resolved room temperature PL measurements of bare ZnO NWs and ZnO / TiO_2 core-shell NW heterostructures annealed at 350 °C for 3 hours in air are presented in **Figures 7** and **8**. The PL mapping shows that, for both samples, the spectra are composed of a sharp near-band edge (NBE) emission centered at 375 nm (*i.e.*, 3.31 eV) and of a broad and more intense visible emission band lying in the range of 500 - 750 nm (*i.e.*, 1.65 – 2.48 eV). The NBE emission is related to radiative bimolecular recombination processes involving neutral donor bound A-excitons, typically through the I_4 and I_5 lines labeled in the I nomenclature[37] that are assigned to substitutional hydrogen on the oxygen lattice site (H_O)[38] and zinc vacancy – hydrogen (V_{Zn}-3H) defect complexes,[39] respectively. The involvement of interstitial hydrogen in bond-centered sites (H_{BC}) is also expected in the NBE emission.[38] The present hydrogen-related defects originating from the crystallization process of bare ZnO NWs in aqueous solution act as shallow donors and thus are responsible for their high electrical conductivity.[40] In contrast, the broad visible emission band from the red/orange to yellow/green

region stems from radiative processes involving electron-hole recombination mediated by deeper states in the bandgap of ZnO NWs. Its assignment has been a long debate over the last two decades and often attributed to oxygen vacancies for explaining the sensing properties of ZnO NWs.[41] The most recent DFT calculations have however established that the emission energies related to oxygen vacancies are smaller than 1 eV and thus cannot account for the present visible emission band obtained by optical spectroscopy.[42] Instead, zinc vacancies as well as (V_{Zn}-H) and (V_{Zn}-2H) defect complexes[42-43] creating deeper states are involved both in the bulk of ZnO NWs and on their surfaces to account for the red/orange/yellow and green/blue emission bands, respectively. Additionally, zinc dangling bonds have recently been associated with an emission energy around 2.41 eV.[42] They may thus contribute also to the visible emission band here through their location on the surfaces of bare ZnO NWs. Interestingly, these two different radiative processes taking place in ZnO NWs are drastically modified when their surfaces are protected by the epitaxial TiO_2 shell grown by ALD and crystallized by post-deposition thermal treatment in air. First, the intensity of the NBE emission is strongly enhanced. This is the result of a reduction of the monomolecular non-radiative recombination processes, which are in this case rather a surface-dominant mechanism than a bulk process owing to the high aspect ratio of ZnO NWs. Second, the broad visible emission band has almost vanished. This result is particularly insightful as it highlights that the hydrogen-related defects in the bulk of ZnO NWs are redistributed following the post-deposition thermal treatment in air while the one on their surfaces very likely get passivated by the epitaxial anatase-TiO_2 shell. These results clarify the origin of the enhancements widely reported in the literature through ZnO/TiO_2 core-shell NW heterostructures. In particular, the epitaxial TiO_2 shell affords to reduce the energy losses from the excited states of ZnO NWs through the passivation of surface defects, thus enhancing cell photo-voltage and charge carrier collection efficiency in photo-electrochemical devices.

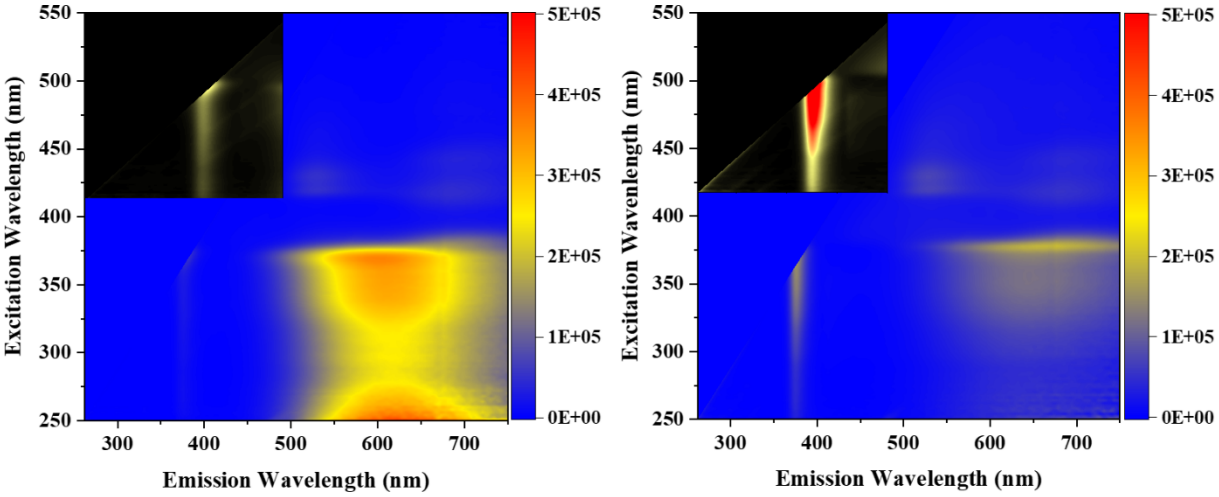


Figure 7. Steady-state room temperature PL measurements of bare ZnO NWs (left) and ZnO / TiO_2 core-shell NW heterostructure annealed at 350 °C for 3 hours in air (right) as a function of the excitation wavelength. The black inset corresponds to a 5 times zoom-in in intensity of the portion below 450 nm to better show the weaker NBE emission for sake of clarity.

The dynamic of these two radiative processes was investigated by time-correlated single photon counting (TCSPC) experiments. The two samples were excited at 375 nm and the PL decays were measured either in the end tail of the sharp NBE emission at 420 nm (**Figure 8 a-b**) or within the broad emission band in the visible range at 610 nm (**Figure 8 c-d**). The evolution of the PL intensity I(t) as a function of the delay time *t* systematically requires three simple exponential components to accurately account for the decays, as follows:

$$I(t) = \sum_{k=1}^{n=3} f_k \, e^{-\left(\frac{t}{\tau_k}\right)}$$

where f_k is the fraction of the k^{th} process, and τ_k is the lifetime of the k^{th} process.

Although the origin of these three contributions can be debated, we favored such a mathematical function rather than a stretch bi-exponential for which the origin of lifetime distribution is also questionable. The two aforementioned radiative processes have a thoroughly different dynamic, as one could expect from their distinct origin. The decay from the NBE emission involving shallow donors is significantly faster than through the deeper traps in the visible emission band,

as reported in **Table 1**. A fast component of ca. 70 ps is deduced for the NBE emission, in addition to a second component at ca. 1 ns and a third component at ca. 8.3 ns, this latter representing the predominant contribution to the decay. The presence of the epitaxial TiO_2 shell slightly accelerates the PL decay and significantly promotes the fast component with a fraction increasing from 11.4 % to 32.16 %. This suggests the possibility of a photon-induced electron transfer from the ZnO NW core towards the epitaxial TiO_2 shell. The PL contribution from the TiO_2 shell is however not detected in our case, thus suggesting a process faster than the time resolution offered by TCSPC. By probing the visible emission band at 610 nm, the faster component of ca. 1.4 ns to the decay is found to be much longer. The second and third components have a lifetime of ca. 7.4 ns and ca. 54.2 ns, respectively, this latter being the major contribution to the decay. In this case, the epitaxial TiO_2 shell does not influence significantly the excited state dynamic of ZnO NWs. This can be anticipated since the deeper position of the states located in the bandgap of ZnO NWs cannot afford any electron transfer towards the TiO_2 shell. Overall, these optical measurements indicate that the epitaxial TiO_2 shell grown by ALD leads to an efficient passivating effect of the surfaces of ZnO NWs as well as to a redistribution of hydrogen-related defects following the post-deposition thermal treatment.

Excitation at 375 nm / Emission at 420 nm							
	τ_1 (ns)	**f_1 (%)**	**τ_2 (ns)**	**f_2 (%)**	**τ_3 (ns)**	**f_3 (%)**	**χ^2**
ZnO	0.069	11.40	0.996	25.17	8.32	63.42	1.060
ZnO/TiO₂	0.067	32.16	0.724	27.85	6.70	39.98	1.149
Excitation at 375 nm / Emission at 610 nm							
	τ_1 (ns)	**f_1 (%)**	**τ_2 (ns)**	**f_2 (%)**	**τ_3 (ns)**	**f_3 (%)**	**χ^2**
ZnO	1.436	14.6	7.445	29.43	54.154	55.96	1.003
ZnO/TiO₂	1.552	5.70	8.852	26.03	53.543	68.27	1.026

Table 1. Lifetime τ_k and fraction f_k values of the k^{th} processes obtained after reconvolution of the instrumental response function for bare ZnO NWs and ZnO / TiO_2 core-shell NW

heterostructures annealed at 350 °C for 3 hours in air for an excitation wavelength at 375 nm and emission wavelengths at 420 nm or 610 nm. χ^2 is the chi value of the fit.

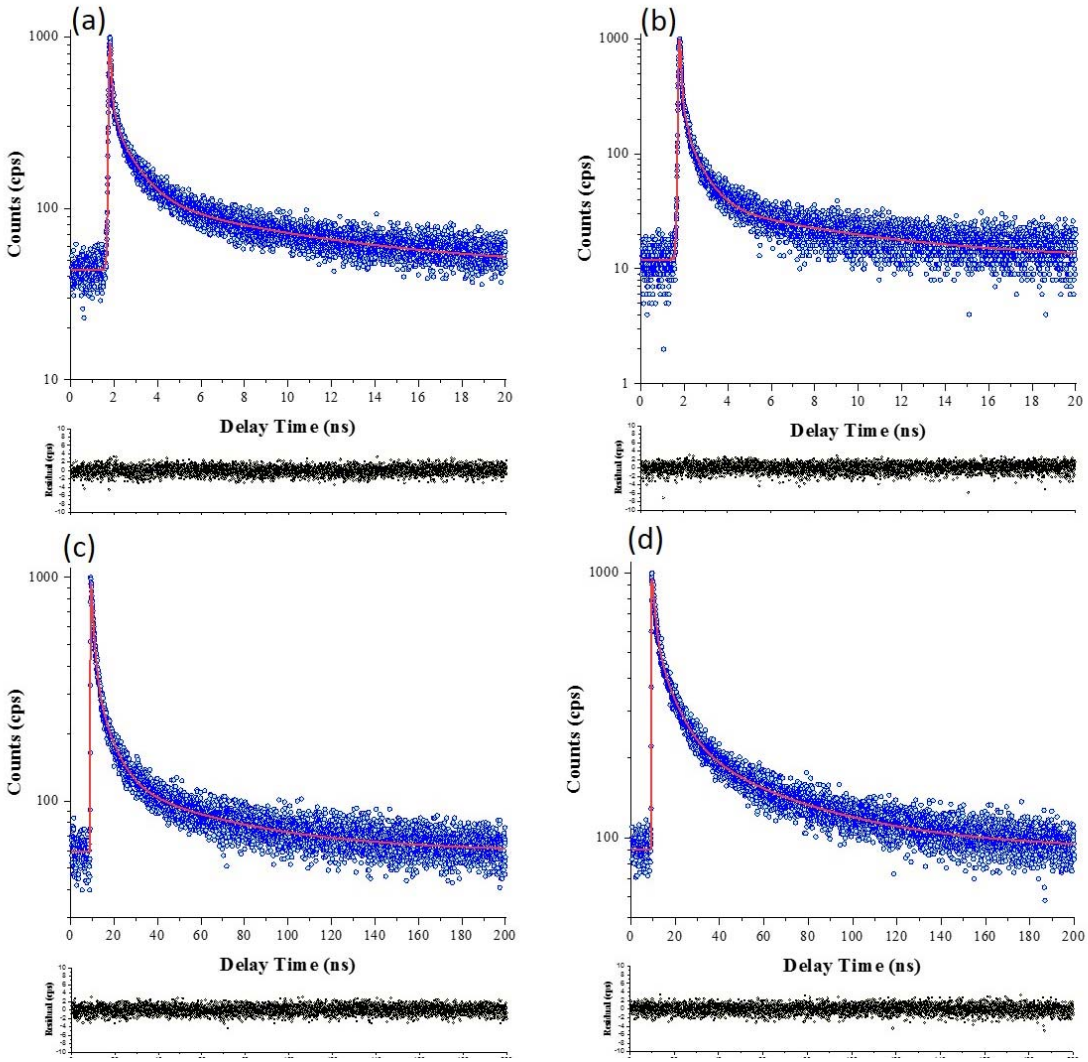


Figure 8. Time-resolved PL decay for (a,c) bare ZnO NWs and (b,d) ZnO / TiO_2 core-shell NW heterostructures annealed at 350 °C for 3 hours in air for an excitation wavelength at 375 nm and emission wavelengths at (a,b) 420 nm or (c,d) 610 nm (laser repetition of 2 MHz, energy of 100 nJ/cm^2, long pass filter of 410 nm). The blue dots correspond to the experimental data and the red curve to the experimental fits after reconvolution of the instrumental response function. The residual is reported at the bottom of each decay.

4. CONCLUSIONS

The chemical instability of ZnO NWs over a broad range of conditions in solution and gas phases as well as the high density of traps on their surfaces require the development of protective, passivating shells for improving their technological integration and maximizing the performances of the related devices. We have developed a double-step process using ALD and post-deposition thermal treatment in air to form a conformal, epitaxial TiO_2 shell on the ZnO NWs with a range of orientation relationships, as shown by TEM-based experiments. The crystallization process has been found to start around 280 °C in air through the formation of the only anatase phase, using an *in situ* analysis combining temperature-dependent Raman scattering and XRD measurements. Furthermore, the epitaxial TiO_2 shell has been revealed to induce a beneficial passivating effect and to redistribute the hydrogen-related defects in the center of ZnO NWs following the post-deposition thermal treatment at 350 °C in air. The optimal conditions for the double-step process are thus compatible with the use of glass covered with a transparent conductive oxide layer as a typical substrate in the field of photovoltaics. These findings report a powerful tool to form ZnO / TiO_2 core-shell NW heterostructures with high structural and optical quality. They further open the way for developing the double-step process in other nanostructured material systems to master the related surface and interface properties.

ASSOCIATED CONTENT

XRD pattern of as-deposited ZnO / TiO_x core-shell NW heterostructures and corresponding XRD patterns obtained after annealing at 250, 350 and 500 °C for 3 hours in air (Figure S1); Raman spectrum of as-deposited ZnO / TiO_x core-shell NW heterostructures and corresponding Raman spectra collected after annealing at 250, 350 and 500 °C for 3 hours in air (Figure S2).

AUTHOR INFORMATION

Corresponding Author

*E-mail : vincent.consonni@grenoble-inp.fr

ACKNOWLEDGEMENTS

The authors acknowledge the financial support by the French Research National Agency through the project DOSETTE (ANR-17-CE24-0004). Funding by Cross-Disciplinary Program of the IDEX Université Grenoble Alpes (ANR-15-IDEX-02) through the project ECO-SESA is also acknowledged. The authors further acknowledge the facilities, and the scientific and technical assistance of the CMTC characterization platform of Grenoble INP, which is supported by the Centre of Excellence of Multifunctional Architectured Materials (LabEx CEMAM) under the contract ANR-10-LABX-44-01 funded by the "Investments for the Future" Program.

REFERENCES

1. Wang, Z. L. Towards Self-Powered Nanosystems: From Nanogenerators to Nanopiezotronics. *Adv. Funct. Mater.* **2008**, *18*, 3553-3567.
2. Willander, M.; Nur, O.; Zhao, Q. X.; Yang, L. L.; Lorenz, M.; Cao, B. Q.; Zuniga-Perez, J.; Czekalla, C.; Zimmermann, G.; Grundmann, M.; et al. Zinc Oxide Nanorod Based Photonic Devices: Recent Progress in Growth, Light Emitting Diodes and Lasers. *Nanotechnology* **2009**, *20*, 40.
3. Tian, W.; Lu, H.; Li, L. Nanoscale Ultraviolet Photodetectors Based on One-Dimensional Metal Oxide Nanostructures. *Nano Res.* **2015**, *8*, 382-405.
4. Consonni, V.; Briscoe, J.; Karber, E.; Li, X.; Cossuet, T. ZnO Nanowires for Solar Cells: A Comprehensive Review. *Nanotechnology* **2019**, *30*, 41.
5. Zhu, L.; Zeng, W. Room-Temperature Gas Sensing of ZnO-Based Gas Sensor: A Review. *Sens. Actuator A-Phys.* **2017**, *267*, 242-261.
6. Zhao, Q. X.; Yang, L. L.; Willander, M.; Sernelius, B. E.; Holtz, P. O. Surface Recombination in ZnO Nanorods Grown by Chemical Bath Deposition. *J. Appl. Phys.* **2008**, *104*, 6.
7. Donatini, F.; Bugallo, A. D.; Tchoulfian, P.; Chicot, G.; Sartel, C.; Sallet, V.; Pernot, J. Comparison of Three E-Beam Techniques for Electric Field Imaging and Carrier Diffusion Length Measurement on the Same Nanowires. *Nano Lett.* **2016**, *16*, 2938-2944.
8. Wang, J.; Liu, X. L.; Yang, A. L.; Zheng, G. L.; Yang, S. Y.; Wei, H. Y.; Zhu, Q. S.; Wang, Z. G. Measurement of Wurtzite ZnO/Rutile TiO_2 Heterojunction Band Offsets by X-Ray Photoelectron Spectroscopy. *Appl. Phys. A-Mater. Sci. Process.* **2011**, *103*, 1099-1103.
9. Law, M.; Greene, L. E.; Radenovic, A.; Kuykendall, T.; Liphardt, J.; Yang, P. D. ZnO-Al_2O_3 and ZnO-TiO_2 Core-Shell Nanowire Dye-Sensitized Solar Cells. *J. Phys. Chem. B* **2006**, *110*, 22652-22663.
10. Wang, M. ; Huang, C.; Cao, Y.; Yu, Q.; Deng, Z.; Liu, Y.; Huang, Z.; Huang, J.; Huang, Q.; Guo, W.; et al. Dye-Sensitized Solar Cells Based on Nanoparticle-Decorated ZnO/TiO_2 Core/Shell Nanorod Arrays. *J. Phys. D-Appl. Phys.* **2009**, *42*, 6.
11. Xu, C. K.; Wu, J. M.; Desai, U. V.; Gao, D. Multilayer Assembly of Nanowire Arrays for Dye-Sensitized Solar Cells. *J. Am. Chem. Soc.* **2011**, *133*, 8122-8125.

12. Prabakar, K.; Son, M.; Kim, W. Y.; Kim, H. TiO_2 Thin Film Encapsulated ZnO Nanorod and Nanoflower Dye Sensitized Solar Cells. *Mater. Chem. Phys.* **2011**, *125*, 12-14.
13. Irannejad, A., Janghorban, K.; Tan, O. K.; Huang, H.; Lim, C. K.; Tan, P. Y.; Fang, X.; Chua, C. S.; Maleksaeedi, S.; Hejazi, S. M. H.; et al. Effect of the TiO_2 Shell Thickness on the Dye-Sensitized Solar Cells with ZnO-TiO_2 Core-Shell Nanorod Electrodes. *Electrochim. Acta* **2011**, *58*, 19-24.
14. Feng, Y. ; Ji, X.; Duan, J.; Zhu, J.; Jiang, J.; Ding, H.; Meng, G.; Ding, R.; Liu, J.; Hu, A.; et al. Synthesis of ZnO@TiO_2 Core-Shell Long Nanowire Arrays and Their Application on Dye-Sensitized Solar Cells. *J. Solid State Chem.* **2012**, *190*, 303-308.
15. Zhao, R.; Zhu, L. P.; Cai, F. P.; Yang, Z. G.; Gu, X. Q.; Huang, J.; Cao, L. ZnO/TiO_2 Core-Shell Nanowire Arrays for Enhanced Dye-Sensitized Solar Cell Efficiency. *Appl. Phys. A-Mater. Sci. Process.* **2013**, *113*, 67-73.
16. Goh, G. K. L.; Le, H. Q.; Huang, T. J.; Hui, B. T. T. Low Temperature Grown ZnO@TiO_2 Core Shell Nanorod Arrays for Dye Sensitized Solar Cell Application. *J. Solid State Chem.* **2014**, *214*, 17-23.
17. Parize, R.; Katerski, A.; Gromyko, I.; Rapenne, L.; Roussel, H.; Karber, E.; Appert, E.; Krunks, M.; Consonni, V. ZnO/TiO_2/Sb_2S_3 Core-Shell Nanowire Heterostructure for Extremely Thin Absorber Solar Cells. *J. Phys. Chem. C* **2017**, *121*, 9672-9680.
18. Cheng, J. J.; Chuang, C. H. M.; Hentz, O.; Rekemeyer, P. H.; Bawendi, M. G.; Gradecak, S. Dimension- and Surface-Tailored ZnO Nanowires Enhance Charge Collection in Quantum Dot Photovoltaic Devices. *ACS Appl. Energy Mater.* **2018**, *1*, 1815-1822.
19. Greene, L. E.; Law, M.; Yuhas, B. D.; Yang, P. D. ZnO-TiO_2 Core-Shell Nanorod/P3HT Solar Cells. *J. Phys. Chem. C* **2007**, *111*, 18451-18456.
20. Lee, Y. J.; Lloyd, M. T.; Olson, D. C.; Grubbs, R. K.; Lu, P.; Davis, R. J.; Voigt, J. A.; Hsu, J. W. P. Optimization of ZnO Nanorod Array Morphology for Hybrid Photovoltaic Devices. *J. Phys. Chem. C* **2009**, *113*, 15778-15782.
21. Atienzar, P.; Ishwara, T.; Illy, B. N.; Ryan, M. P.; O'Regan, B. C.; Durrant, J. R.; Nelson, J. Control of Photocurrent Generation in Polymer/ZnO Nanorod Solar Cells by Using a Solution-Processed TiO_2 Overlayer. *J. Phys. Chem. Lett.* **2010**, *1*, 708-713.
22. Son, D. Y.; Bae, K. H.; Kim, H. S.; Park, N. G. Effects of Seed Layer on Growth of ZnO Nanorod and Performance of Perovskite Solar Cell. *J. Phys. Chem. C* **2015**, *119*, 10321-10328.
23. Wang, B. X.; Liu, T. F.; Zhou, Y. B.; Chen, X.; Yuan, X. B.; Yang, Y. Y.; Liu, W. P.; Wang, J. M.; Han, H. W.; Tang, Y. W. Hole-Conductor-Free Perovskite Solar Cells with Carbon Counter Electrodes Based on ZnO Nanorod Arrays. *Phys. Chem. Chem. Phys.* **2016**, *18*, 27078-27082.
24. Wang, Y.; Zheng, Y. Z.; Lu, S. Q.; Tao, X.; Che, Y. K.; Chen, J. F. Visible-Light-Responsive TiO_2-Coated ZnO:I Nanorod Array Films with Enhanced Photoelectrochemical and Photocatalytic Performance. *ACS Appl. Mater. Interfaces* **2015**, *7*, 6093-6101.
25. Mukhopadhyay, S.; Maiti, D.; Chatterjee, S.; Devi, P. S.; Kumar, G. S. Design and Application of Au Decorated ZnO/TiO_2 as a Stable Photocatalyst for Wide Spectral Coverage. *Phys. Chem. Chem. Phys.* **2016**, *18*, 31622-31633.
26. Parize, R.; Cossuet, T.; Appert, E.; Chaix-Pluchery, O.; Roussel, H.; Rapenne, L.; Consonni, V. Synthesis and Properties of ZnO/TiO_2/Sb_2S_3 Core-Shell Nanowire Heterostructures Using the Silar Technique. *Crystengcomm* **2018**, *20*, 4455-4462.
27. Guillemin, S.; Appert, E.; Roussel, H.; Doisneau, B.; Parize, R.; Boudou, T.; Bremond, G.; Consonni, V. Controlling the Structural Properties of Single Step, Dip Coated ZnO Seed Layers for Growing Perfectly Aligned Nanowire Arrays. *J. Phys. Chem. C* **2015**, *119*, 21694-21703.
28. Parize, R.; Garnier, J.; Chaix-Pluchery, O.; Verrier, C.; Appert, E.; Consonni, V. Effects of Hexamethylenetetramine on the Nucleation and Radial Growth of ZnO Nanowires by Chemical Bath Deposition. *J. Phys. Chem. C* **2016**, *120*, 5242-5250.
29. Cusco, R.; Alarcon-Llado, E.; Ibanez, J.; Artus, L.; Jimenez, J.; Wang, B. G.; Callahan, M. J. Temperature Dependence of Raman Scattering in ZnO. *Phys. Rev. B* **2007**, *75*, 11.
30. Chang, H.; Huang, P. J. Thermo-Raman Studies on Anatase and Rutile. *J. Raman Spectrosc.* **1998**, *29*, 97-102.

31. Du, Y. L.; Deng, Y.; Zhang, M. S. Variable-Temperature Raman Scattering Study on Anatase Titanium Dioxide Nanocrystals. *J. Phys. Chem. Solids* **2006**, *67*, 2405-2408.
32. Rauch, E. F.; Veron, M. Automated Crystal Orientation and Phase Mapping in Tem. *Mater. Charact.* **2014**, *98*, 1-9.
33. Midgley, P. A.; Eggeman, A. S. Precession Electron Diffraction - a Topical Review. *IUCrJ* **2015**, *2*, 126-136.
34. Consonni, V.; Rapenne, L.; Renou, G.; Roussel, H.; Gerard, L.; Cusco, R.; Artus, L.; Andre, R.; Rauch, E. F. Identifying and Mapping the Polytypes and Orientation Relationships in ZnO/CdSe Core-Shell Nanowire Arrays. *Nanotechnology* **2016**, *27*, 12.
35. Yang, Y.; Scholz, R.; Fan, H. J.; Hesse, D.; Gosele, U.; Zacharias, M. Multitwinned Spinel Nanowires by Assembly of Nanobricks Via Oriented Attachment: A Case Study of Zn_2TiO_4. *ACS Nano* **2009**, *3*, 555-562.
36. Vasu, K.; Sreedhara, M. B.; Ghatak, J.; Rao, C. N. R. Atomic Layer Deposition of P-Type Epitaxial Thin Films of Undoped and N-Doped Anatase TiO_2. *ACS Appl. Mater. Interfaces* **2016**, *8*, 7897-7901.
37. Meyer, B. K.; Alves, H.; Hofmann, D. M.; Kriegseis, W.; Forster, D.; Bertram, F.; Christen, J.; Hoffmann, A.; Strassburg, M.; Dworzak, M.; et al. Bound Exciton and Donor-Acceptor Pair Recombinations in ZnO. *Phys. Status Solidi B-Basic Solid State Phys.* **2004**, *241*, 231-260.
38. Lavrov, E. V.; Herklotz, F.; Weber, J. Identification of Two Hydrogen Donors in ZnO. *Phys. Rev. B* **2009**, *79*, 13.
39. Heinhold, R.; Neiman, A.; Kennedy, J. V.; Markwitz, A.; Reeves, R. J.; Allen, M. W. Hydrogen-Related Excitons and Their Excited-State Transitions in ZnO. *Phys. Rev. B* **2017**, *95*, 13.
40. Cossuet, T.; Donatini, F.; Lord, A. M.; Appert, E.; Pernot, J.; Consonni, V. Polarity-Dependent High Electrical Conductivity of ZnO Nanorods and Its Relation to Hydrogen. *J. Phys. Chem. C* **2018**, *122*, 22767-22775.
41. Barbagiovanni, E. G.; Reitano, R.; Franzo, G.; Strano, V.; Terrasi, A.; Mirabella, S. Radiative Mechanism and Surface Modification of Four Visible Deep Level Defect States in ZnO Nanorods. *Nanoscale* **2016**, *8*, 995-1006.
42. Lyons, J. L.; Varley, J. B.; Steiauf, D.; Janotti, A.; Van de Walle, C. G. First-Principles Characterization of Native-Defect-Related Optical Transitions in ZnO. *J. Appl. Phys.* **2017**, *122*, 12.
43. Frodason, Y. K.; Johansen, K. M.; Bjorheim, T. S.; Svensson, B. G.; Alkauskas, A. Zn Vacancy-Donor Impurity Complexes in ZnO. *Phys. Rev. B* **2018**, *97*, 8.

GRAPHICAL CONTENT

